Improving the efficiency of open-quantum-system simulations using matrix product states in the interaction picture

Kai T. Liu, David N. Beratan, 1,2,3,* and Peng Zhang, 1
Department of Chemistry, Duke University, Durham, North Carolina 27708, USA
Department of Biochemistry, Duke University, Durham, North Carolina 27710, USA
Department of Physics, Duke University, Durham, North Carolina 27708, USA

(Received 29 November 2021; accepted 9 February 2022; published 3 March 2022)

Modeling open quantum systems—quantum systems coupled to a bath—is of value in condensed-matter theory, cavity quantum electrodynamics, nanosciences, and biophysics. The real-time simulation of open quantum systems was advanced significantly by the recent development of chain mapping techniques and the use of matrix product states that exploit the intrinsic entanglement structure in open quantum systems. The computational cost of simulating open quantum systems, however, remains high when the bath is excited to high-lying quantum states. We develop an approach to reduce the computational costs in such cases. The interaction representation for the open quantum system is used to distribute excitations among the bath degrees of freedom so that the occupation of each bath oscillator is ensured to be low. The interaction picture also causes the matrix dimensions to be much smaller in a matrix product state of a chain-mapped open quantum system than in the Schrödinger picture. Using the interaction representation accelerates the calculations by one to two orders of magnitude over the existing matrix-product-state method. In the regime of strong system-bath coupling and high temperatures, the speedup can be as large as three orders of magnitude. The approach developed here is especially promising to simulate the dynamics of open quantum systems in high-temperature and strong-coupling regimes.

DOI: 10.1103/PhysRevA.105.032406

I. INTRODUCTION

The density-matrix renormalization-group (DMRG) method [1] has become a standard tool to study low-dimensional systems, especially one- and two-dimensional spin systems [2,3]. The essence of the DMRG method is to retain the most significant states associated with the relevant properties of a quantum system and discard the less important ones using singular values decomposition. The time-dependent version of DMRG (t-DMRG) [4–6] is promising to describe quantum dynamics and it can achieve high accuracy at moderate computational cost. The DMRG and t-DMRG methods are most easily understood using the language of the matrix-product-state (MPS) [7–10] representation of quantum states.

The MPS representation was developed to describe onedimensional systems, including the Ising model and its variants [2] and the Bose-Hubbard model [11]. Using t-DMRG to study the condensed-phase quantum dynamics of electron or energy transfer, for example, requires that the electron-vibration Hamiltonian be mapped onto one dimension, although the electron-vibration Hamiltonian has an intrinsic star-shaped topology [12,13]—the electronic system interacts with all of the vibrational modes present (see Fig. 1). The requirement of t-DMRG for a one-dimensional (1D) configuration is fulfilled by arranging the bath modes along a line and placing the electronic system at the end of the line, as shown in Fig. 1. This configuration is known as the star geometry [14,15]. Using the star geometry does not change the content of an electron-vibration Hamiltonian, and it places the electronic system and the bath modes into a one-dimension topology, introducing long-range interactions between the electronic system and the bath modes (Fig. 2). Despite the long-range interactions, the star geometry was proven to be efficient when calculating the Green's functions of a special open quantum system (for example, the Anderson impurity models where the impurity, a magnetic atom, is the quantum system and the conduction electrons are the bath) at zero temperature in the context of MPS [16].

For open quantum systems other than the impurity model, the star geometry is not necessarily efficient numerically, because it involves long-range interactions. Long-range interactions are believed to make MPS simulations computationally expensive because the bond dimensions (i.e., the number of important singular values of the density matrix) in a MPS grows, in general, rapidly as a function of time. In addition, the effect of finite temperatures on the numerical efficiency of the star geometry and the chain geometry is not clear. The recently developed approach of using a thermalized spectral density [17,18] to describe finite temperature open quantum systems maps a finite-temperature bath to an effective zero-temperature bath, and it is not clear whether the star geometry remains efficient in this thermofield description of finite-temperature effects. A strategy that is different from

^{*}david.beratan@duke.edu †peng.zhang@duke.edu.

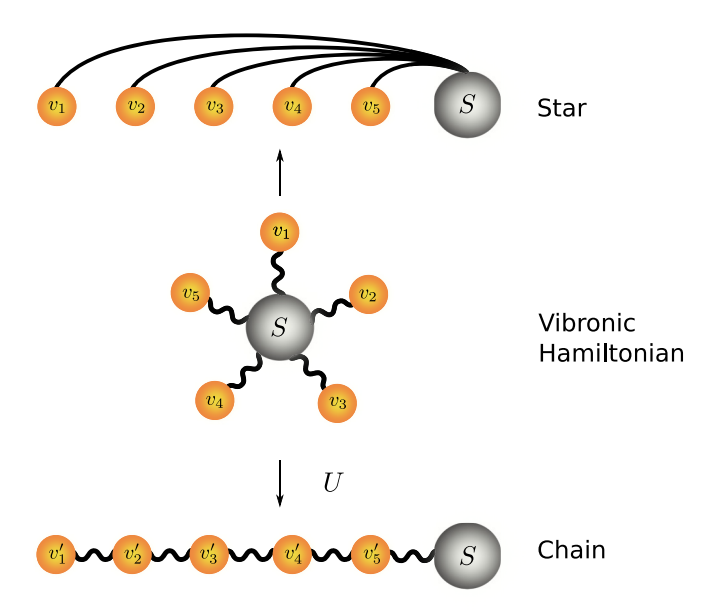


FIG. 1. Configurations of the star and chain geometries. The lines represent the interactions between sites. The star geometry does not change the vibronic Hamiltonian *per se* and it is a 1D representation of the Hamiltonian. The ordering of bath modes is crucial to the efficiency of the star geometry. Ordering by the magnitudes of bath-mode frequencies is commonly used [22]. The chain Hamiltonian is obtained from the vibronic Hamiltonian by a unitary transformation *U* and it contains interaction terms between two adjacent bath modes.

using the star geometry, the chain geometry mapping [19,20], was proposed to avoid the long-range interactions present in the star geometry. The chain geometry differs from the star geometry in the topology of the bath modes (vibrations). In the chain geometry, the bath modes are mapped to a 1D chain of oscillators with nearest-neighbor interactions, and the quantum system interacts only with the first bath mode in the 1D chain. The short-time dynamics of open quantum systems

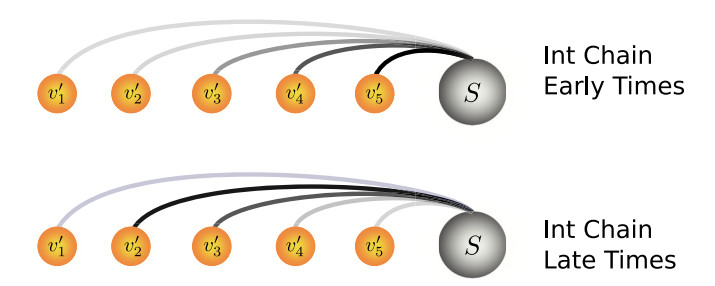


FIG. 2. Configuration of the interaction-picture chain Hamiltonian. In the interaction-picture chain Hamiltonian, the mode-mode terms are removed and the system interacts with all of the modes. An important feature of the interaction-picture Hamiltonian is that the interaction strengths of the system and bath modes are time-dependent and spatially localized. Here, we use the thickness of lines to indicate the interaction strengths. At early times, the system interacts strongly with the first several modes. At later times, the strongest interactions move to further parts of the 1D chain. The interactions are always localized in a narrow band of vibrational modes (see Fig. 5). In contrast, in the star geometry, the interactions are not spatially localized.

can be described largely by a few modes in close proximity to the system [21]. Many quantum dynamical simulations have been performed using the chain geometry, and it is believed that the chain geometry usually (has a lower computational cost) than the star geometry since the bond dimensions of MPS in the chain geometry are small (because the long-range interactions are absent).

Although the bond dimensions in the chain geometry are believed to be smaller than in the star geometry, the computational cost of open-quantum-system simulations with a boson bath also depends on another quantity—the number of eigenstates of each bath mode (i.e., the *local dimension*). When k_BT (T is temperature) is large compared to the energy spacing of the bath modes, the local dimension for each bath mode must be large enough to ensure numerical convergence of the simulations. Similarly, in the strong system-bath coupling regime, large local dimensions for the bath modes are also necessary for numerical convergence. The large local dimensions may slow simulations that use a chain geometry. For example, in the chain geometry, if the dimension of the Hilbert space for a bath mode (local dimension) is 100 (see Sec. IV for an example), an interaction term $\kappa_n(\hat{b}_n^{\dagger}\hat{b}_{n-1} + \text{H.c.})$, where b_n^{\dagger} is the creation operator for the *n*th mode in the chain, generates an evolution operator with a corresponding matrix of the size $10^4 \times 10^4$, causing time-consuming matrix operations. Furthermore, large local dimensions of bath modes also significantly affect the size of the tensors in a MPS because the dimension of one of the indices in a MPS tensor is equal to the local dimension of the corresponding site (here, a bath mode). The large tensors in MPS then make the required singular value decomposition a difficult task. In summary, when using the chain geometry, the dimensions of the evolution matrices or of the Hamiltonian matrices become large at high temperatures or in the strong-coupling regime, and the corresponding numerical simulations in these regimes become impractical. This large-matrix problem does not exist in the star geometry because the system is often described by a smaller Hilbert space than the bath modes, and the interaction terms in the star geometry couple the system to each bath mode, making the matrix size much smaller than in the chain geometry. However, the bond dimensions in the star geometry grow rapidly with time since long-range interactions induce strong entanglement, which makes long-time simulations challenging. The small dimension of the interaction terms in the star geometry motivate us to transform the interaction terms in the chain geometry to resolve the large-matrix difficulty that impedes the chain-geometry simulations, especially in the regimes of high temperatures and strong system-bath interactions.

Now, we describe an approach to overcome the computational challenges of the chain and star geometries by transforming the chain Hamiltonian to the interaction picture. In the interaction picture, the transformed Hamiltonian does not contain the mode-mode interaction terms, thus producing much smaller evolution matrices. The transformed chain Hamiltonian features a star geometry with time-dependent system-bath couplings. In contrast to the star geometry in the Schrödinger picture, the time-dependent couplings are spatially localized, producing slower growth of entanglement.

We use the transformed chain geometry in the interaction picture to describe the spin-boson model and compare the resulting dynamics, bond dimensions, and computational costs to the treatment with the Schrödinger-picture chain and star geometries. Efficient methods were published recently that go beyond the direct simulations of the system and discretized bath that are used in the present study. Instead, they use the pseudomode–effective-mode description of baths [23,24] or use a novel description of non-Markovianity of open systems [25], which significantly extends the accessible simulation time of open systems. The relationship between the interaction-picture transformation reported here and those alternative methods is an interesting topic for further explorations.

The paper is organized as follows. Section II derives the full and the truncated (finite chain length) form of the chain-geometry Hamiltonian in the interaction picture. The truncated form is used for the spin-boson model simulations. Section IV compares the results obtained with the chaingeometry Hamiltonian in the interaction picture, the chain geometry in the Schrödinger picture, and the star geometry. These studies demonstrate the speed and accuracy of the interaction-picture chain geometry approach. Using scaling analysis, we show that the interaction-picture chain geometry approach is 1–2 orders of magnitude faster than the other two schemes if the vibrational mode excitations are high. The strategy developed here allows the use of t-DMRG and tensor networks to simulate strongly coupled vibronic systems in the high-temperature regime $(k_B T \gg \hbar \omega_c)$, where ω_c is the characteristic frequency of the bath), such as the strong-coupling-enabled nonthermal coupled electron-exciton transport (quantum ratcheted reactions [26]) and ambienttemperature excitation energy transfer reactions, for example. This method is also suitable to model ultrastrong coupling and deep-strong-coupling regimes (for a description of these regimes, see Refs. [27,28]) in light-matter interactions [29]. Section V summarizes features of the computational scheme (chain geometry in the interaction picture) and discusses possible improvements to this scheme.

II. THEORY AND METHODOLOGY

A. Orthogonal polynomial mapping of the Hamiltonian

The Hamiltonian in Eq. (1) describes a quantum system coupled to a bath (i.e., an open quantum system) with $\hbar = 1$,

$$H = H_s + H_{sb} + H_b$$

$$= H_s + A_s \otimes \int_{\Omega_0}^{\Omega_1} (\hat{a}_{\omega}^{\dagger} + \hat{a}_{\omega}) h(\omega) d\omega$$

$$+ \int_{\Omega}^{\Omega_1} \hat{a}_{\omega}^{\dagger} \hat{a}_{\omega} \omega d\omega.$$
(2)

 $\hat{a}_{\omega}^{\dagger}$ and \hat{a}_{ω} are the creation and annihilation operators for a boson mode of frequency ω . $h(\omega)$ is the coupling strength between the system and the bath mode of frequency ω . The frequencies Ω_0 and Ω_1 are the upper and lower limits of the bath frequencies. When T>0 K, the spectral density has a temperature-dependent form $J(\omega,\beta)=\mathrm{sgn}(\omega)J(|\omega|)[1+\mathrm{coth}(\beta\omega/2)]/2$ with $\beta=1/k_BT$, and the lower limit Ω_0 is extended to $-\infty$ because negative-frequency bath modes are needed to construct the Boltzmann distribution of bath

states [17,30]. Thus, at finite temperatures, $h(\omega)$ also becomes temperature dependent: $h(\omega, \beta) = \sqrt{J(\omega, \beta)}$. When the temperature is 0 K, $h(\omega) = \sqrt{J(\omega)}$ where $J(\omega)$ is the spectral density with $0 < \omega < \infty$ because no negative-frequency bath modes are needed to construct the Boltzmann distribution.

The Hamiltonian in Eq. (2) with a continuous distribution of bath frequencies can be transformed to a discrete nearest-neighbor form [Eq. (3)] by a unitary transformation $U_n(\omega) = h(\omega)p_n(\omega)$, where $p_n(\omega)$ is a set of real, continuous, orthogonal, and normalized polynomials generated by the weight function $h^2(x)$ [19,31],

$$\tilde{H} = H_s + \underbrace{\kappa_0 A_s \otimes (\hat{b}_0 + \hat{b}_0^{\dagger})}_{\hat{H}_{sb}} + \underbrace{\sum_{n=0}^{\infty} \omega_n b_n^{\dagger} \hat{b}_n + \sum_{n=1}^{\infty} \kappa_n (\hat{b}_n^{\dagger} \hat{b}_{n-1} + \text{H.c.})}_{\hat{H}_b}.$$
 (3)

 \hat{b}_n is a linear combination of \hat{a}_n . In the transformed Hamiltonian, the system only interacts with the zeroth mode $(\hat{b}_0, \hat{b}_0^{\dagger})$.

The linear transformation U relates $\hat{a}^{\dagger}_{\omega}$ and \hat{b}^{\dagger}_{n} :

$$\hat{a}_{\omega}^{\dagger} = \sum_{n=0}^{\infty} U_n(\omega) \hat{b}_n^{\dagger} = \sum_{n=0}^{\infty} h(\omega) p_n(\omega) b_n^{\dagger}, \tag{4}$$

where \hat{b}_n^{\dagger} and \hat{b}_n are the creation and annihilation operators for mode n of the chain. The orthonormal polynomials $p_n(\omega)$ satisfy the recurrence relation

$$p_{n+1}(x) = (C_n x - A_n) p_n(x) - B_n p_{n-1}(x), \quad n = 0, 1, 2 \dots,$$
(5)

with $p_{-1}(x) = 0$ [31,32]. The coefficients A_n , B_n , C_n are related to the coupling strength κ_n and frequency ω_n [31]:

$$A_n = \frac{\omega_n}{\kappa_{n+1}}, \quad B_n = \frac{\kappa_n}{\kappa_{n+1}}, \quad C_n = \frac{1}{\kappa_{n+1}}, \quad n = 0, 1, 2, \dots$$
 (6)

Using the recurrence relation [Eq. (5)], we can compute $p_n(x)$ given the frequencies ω_n , couplings κ_n , and the first two polynomials $p_{-1}(x) = 0$, $p_0 = 1/\kappa_0 = 1/\sqrt{\int_{\Omega_0}^{\Omega_1} h^2(x) dx}$. The recurrence relations, the relationships among ω_n , κ_n , A_n , B_n , and C_n , and the properties of the orthogonal polynomials are described in Refs. [19,31].

B. Chain Hamiltonian in the interaction picture

 \tilde{H} in Eq. (3) is the chain Hamiltonian that contains couplings between two adjacent bath modes. H in Eq. (2) is the star Hamiltonian. The time evolution of the system and bath is governed by \tilde{H} or H. In the Schrödinger picture, the time evolution is

$$|\psi(t)\rangle_S = e^{-i\tilde{H}t} |\psi(0)\rangle_S.$$
 (7)

By transforming the chain Hamiltonian to the interaction picture, the coupling terms between adjacent bath modes are removed and only the system-bath couplings and the system operator remain, as we will show. The dimensions of the Hamiltonian matrices that describe these system-bath coupling terms are much smaller than the mode-mode coupling terms in the Schrödinger picture, since the dimension of the system Hilbert space is often small [33–35] (equal to 2 for a spin system, for example, while the dimension of a single bath mode can be around 100 [36]). Therefore, we expect that the computational cost of simulating the interaction-picture Hamiltonian in Eq. (3) with MPS can be much lower than that in the Schrödinger-picture chain geometry.

1. Chain Hamiltonian in the interaction picture

In the interaction picture with respect to \tilde{H}_b , the wave function is $|\psi(t)\rangle_I = e^{i\tilde{H}_b t} |\psi(t)\rangle_S$ and the evolution operator $\hat{U}_I(t,0) = e^{i\tilde{H}_b t} e^{-i\tilde{H}t}$, has the time evolution

$$\frac{d}{dt}\hat{U}_I(t,0) = e^{i\tilde{H}_b t}(-i\tilde{H} + i\tilde{H}_b)e^{-i\tilde{H}t}$$

$$=e^{i\tilde{H}_bt}(-i\tilde{H}+i\tilde{H}_b)e^{-i\tilde{H}_bt}e^{i\tilde{H}_bt}e^{-i\tilde{H}t} \qquad (8)$$

$$= -ie^{i\tilde{H}_b t} (H_s + \tilde{H}_{sb}) e^{-i\tilde{H}_b t} \hat{U}_I(t,0). \tag{9}$$

Eq. (9) describes the interaction-picture Hamiltonian $\tilde{H}_I = e^{i\tilde{H}_b t} (H_s + \tilde{H}_{sb}) e^{-i\tilde{H}_b t}$.

It is difficult to begin with $e^{i\tilde{H}_b t}(H_s + \tilde{H}_{sb})e^{-i\tilde{H}_b t}$ to obtain an expansion of \tilde{H}_I in terms of \hat{b}_n and \hat{b}_n^{\dagger} . Instead, we first turn to the star geometry and define the interaction-picture stargeometry Hamiltonian $H_I(t)$ [Eq. (2)] as

$$H_{I}(t) = e^{iH_{b}t}(H_{s} + H_{sb})e^{-iH_{b}t}$$

$$= H_{s} + A_{s} \otimes \int_{\Omega_{a}}^{\Omega_{1}} (\hat{a}_{\omega}^{\dagger} e^{i\omega t} + \hat{a}_{\omega} e^{-i\omega t})h(\omega) d\omega. \quad (10)$$

 $\tilde{H}_I(t)$ and $H_I(t)$ are related by the chain mapping transformation U_n [Eq. (4)] [19]. Therefore,

$$\tilde{H}_I(t) = H_s + A_s \otimes \int_{\Omega_0}^{\Omega_1} \left[\sum_{n=0}^{\infty} U_n(\omega) \hat{b}_n^{\dagger} e^{i\omega t} + \sum_{n=0}^{\infty} U_n(\omega) \hat{b}_n e^{-i\omega t} \right] h(\omega) d\omega$$

$$=H_s+A_s\otimes\sum_{n=0}^{\infty}\left[\hat{b}_n^{\dagger}\int_{\Omega_0}^{\Omega_1}h^2(\omega)p_n(\omega)e^{i\omega t}\,d\omega+\hat{b}_n\int_{\Omega_0}^{\Omega_1}h^2(\omega)p_n(\omega)e^{-i\omega t}\,d\omega\right]$$
(11)

$$= H_s + A_s \otimes \sum_{n=0}^{\infty} [d_n^*(t)\hat{b}_n^{\dagger} + d_n(t)\hat{b}_n]. \tag{12}$$

Here, $d_n(t) = \int_{\Omega_0}^{\Omega_1} h^2(\omega) p_n(\omega) e^{-i\omega t} d\omega$ and $d_n^*(t)$ is the complex conjugate of $d_n(t)$. By definition, $d_n(t)$ is the Fourier transform of $p_n(\omega)$ with the weight function $h^2(\omega)$ for $\Omega_0 < \omega < \Omega_1$.

The evolution operator in the interaction picture is $\hat{U}(t + \delta t, t) = e^{-i \int_t^{t+\delta t} \tilde{H}_I(s) ds}$:

$$U(t + \delta t, t) = \exp\left\{-i\left[H_s\delta t + A_s\right]\right\}$$

$$\otimes \sum_{n=0}^{\infty} [d_n(\omega, t, \delta t)\hat{b}_n + \text{H.c.}]\right\}, \quad (13)$$

where $d_n(\omega, t, \delta t) = \int_{\Omega_0}^{\Omega_1} h^2(\omega) p_n(\omega) (\int_t^{t+\delta t} e^{-i\omega s} ds) d\omega$ and δt is the size of a single evolution step.

2. Truncated form of the chain Hamiltonian in the interaction picture

The Hamiltonian in Eq. (12) describes a semi-infinite chain. In simulations, the semi-infinite chain will be truncated in one of two ways. One approach is to keep the first N terms in the summation of Eq. (12).

The other truncation scheme is easier in the sense that the integrals in Eq. (12) are not needed. It begins with the

truncated form of the original *chain* Hamiltonian (this Hamiltonian is denoted as the C form) Eq. (3):

$$\tilde{H} = H_s + \underbrace{\kappa_0 A_s \otimes (\hat{b}_0 + \hat{b}_0^{\dagger})}_{\tilde{H}_{sb}} + \underbrace{\sum_{n=0}^{N} \omega_n b_n^{\dagger} \hat{b}_n + \sum_{n=1}^{N} \kappa_n (\hat{b}_n^{\dagger} \hat{b}_{n-1} + \text{H.c.})}_{\tilde{B}}.$$
(14)

To transform this Hamiltonian into the interaction picture with respect to \tilde{H}_b , we first diagonalize \tilde{H}_b . The diagonalization uses the fact that \tilde{H}_b can be written as

$$\tilde{H}_b = \mathbf{b}^{\dagger} \mathbf{M} \mathbf{b}, \tag{15}$$

where $\hat{\mathbf{b}}^{\dagger} = (\hat{b}_0^{\dagger}, \dots, \hat{b}_N^{\dagger})$, $\mathbf{b} = (\hat{b}_0, \dots, \hat{b}_N)^T$, and the Lanczos tridiagonal matrix [20] **M** is

$$\mathbf{M} = \begin{pmatrix} \omega_0 & \kappa_1 \\ \kappa_1 & \omega_1 & \kappa_2 \\ & \ddots & \ddots & \ddots \\ & & \kappa_{N-1} & \omega_{N-1} & \kappa_N \\ & & & \kappa_N & \omega_N \end{pmatrix}. \tag{16}$$

M can be diagonalized by the unitary transformation: $\mathbf{M} = \mathbf{P}^{\dagger} \mathbf{A} \mathbf{P}$, where $\mathbf{\Lambda} = \operatorname{diag}(\lambda_0, \dots, \lambda_N)$ is a diagonal matrix with the elements equal to the frequencies of the independent bath modes. Defining $\mathbf{a} = (\hat{a}_0, \dots, \hat{a}_k, \dots, \hat{a}_N)^T = \mathbf{P} \cdot \mathbf{b}$, which implies $\mathbf{b} = \mathbf{P}^{\dagger} \cdot \mathbf{a}$, we transform \tilde{H} to the star Hamiltonian H (denoted as the S form)

$$H = H_s + A_s \otimes \sum_{k=0}^{N} \kappa_0(P_{0,k}^{\dagger} \hat{a}_k + P_{k,0} \hat{a}_k^{\dagger}) + \sum_{k=0}^{N} \lambda_k a_k^{\dagger} \hat{a}_k,$$
(17)

where $P_{k,0}$ is the first column of **P** and $P_{0,k}^{\dagger}$ is the first row of \mathbf{P}^{\dagger} .

The next steps are to transform the Hamiltonian [Eq. (17)] to the interaction picture with respect to the bath Hamiltonian $\sum_{k=0}^{N} \lambda_k a_k^{\dagger} \hat{a}_k$ and then write the ladder operators \hat{a}_k , \hat{a}_k^{\dagger} in terms of the chain geometry ladder operators, namely \hat{b}_n and \hat{b}_n^{\dagger} . The resulting truncated star Hamiltonian in the interaction picture is

$$H_{I} = H_{s} + A_{s} \otimes \sum_{k=0}^{N} \kappa_{0} \left(P_{0,k}^{\dagger} e^{-i\lambda_{k}t} \hat{a}_{k} + P_{k,0} e^{i\lambda_{k}t} \hat{a}_{k}^{\dagger} \right).$$
(18)

Using $\hat{a}_k = \sum_{n=0}^N P_{k,n} \hat{b}_n$ and $\hat{a}_k^{\dagger} = \sum_{n=0}^N P_{n,k}^{\dagger} \hat{b}_n^{\dagger}$ to transform \hat{a}_k , \hat{a}_k^{\dagger} to \hat{b}_n and \hat{b}_n^{\dagger} in Eq. (18) leads to the chain-geometry Hamiltonian in the interaction picture (denoted as the IC form),

$$\tilde{H}_{I} = H_{s} + A_{s} \otimes \sum_{k=0}^{N} \sum_{n=0}^{N} \kappa_{0} \left(P_{0,k}^{\dagger} P_{k,n} e^{-i\lambda_{k}t} \hat{b}_{n} + \text{H.c.} \right)$$
(19)

$$= H_s + A_s \otimes \sum_{n=0}^{N} [d_n(t)\hat{b}_n + \text{H.c.}]$$
 (20)

$$= H_s + H_{s,0}(t) + H_{s,1}(t) + \dots + H_{s,N}(t), \qquad (21)$$

where we define $d_n(t) = \sum_{k=0}^N \kappa_0 P_{0,k}^{\dagger} P_{k,n} e^{-i\lambda_k t}$. In Eq. (21), we also defined $H_{s,n}(t) = A_s \otimes [d_n(t)\hat{b}_n + \text{H.c.}]$. This truncated Hamiltonian of Eq. (21) in the interaction picture is used in the simulations of Sec. IV. The transformation from Eq. (17) to Eq. (21) and the time-dependent couplings associated with the bath modes are reminiscent of the space-dependent couplings and the chain transformation in Ref. [37], where the real-space coordinate of the bath modes plays a similar role as time in Eq. (21).

The one time step evolution operator for the IC Hamiltonian [Eq. (21)] is

$$\hat{U}(t+\delta t,t) = e^{-i[H_s\delta t + \sum_{n=0} H_{s,n}(t+\delta t/2)\delta t]}$$
 (22)

$$= e^{-i\left\{H_s\delta t + A_s\otimes\sum_{n=0}^{N} [d_n(t+\delta t/2)\hat{b}_n\delta t + \text{H.c.}]\right\}}.$$
 (23)

Here, we use the midpoint Hamiltonian $H_{s,n}(t + \delta t/2)$ to approximate the time-dependent Hamiltonians on the interval $[t, t + \delta t]$.

The evolution operator in Eq. (23) is then Troterrized to second order in the time step,

$$U(t + \delta t, t) \approx e^{-i\{H_s + A_s \otimes [d_0(t + \delta t/4)\hat{b}_0 + \text{H.c.}]\} \delta t/2}$$

$$e^{-i\{A_s \otimes [d_1(t + \delta t/4)\hat{b}_1 + \text{H.c.}]\} \delta t/2} \dots$$

$$e^{-i\{A_s \otimes [d_N(t + \delta t/2)\hat{b}_N + \text{H.c.}]\} \delta t/2}$$

$$e^{-i\{A_s \otimes [d_N(t + \delta t/2)\hat{b}_N + \text{H.c.}]\} \delta t/2} \dots$$

$$e^{-i\{A_s \otimes [d_N(t + \delta t/2)\hat{b}_N + \text{H.c.}]\} \delta t/2} \dots$$

$$e^{-i\{A_s \otimes [d_1(t + \delta t/4)\hat{b}_1 + \text{H.c.}]\} \delta t/2}$$

$$e^{-i\{H_s + A_s \otimes [d_0(t + \delta t/4)\hat{b}_0 + \text{H.c.}]\} \delta t/2}. \tag{24}$$

The advantage of using the interaction picture evolution operator [Eq. (24)] is that the dimensions of the evolution matrices are much smaller than those in the original Schrödinger picture for the chain geometry. The original Schrödinger-picture chain Hamiltonian Eq. (14) contains terms, such as $\hat{b}_n\hat{b}_{n-1}$, and the dimension of \hat{b}_n and \hat{b}_{n-1} has to be large enough to ensure convergence. In the interaction picture, in contrast, the Hamiltonian only contains H_s and interaction terms of the form $A_{sys} \otimes [d_n(t)\hat{b}_n + \text{H.c.}]$. Since the dimension of the system is often much smaller than the dimension of the bath vibrational modes $(\hat{b}_n, \hat{b}_n^{\dagger})$, the sizes of the evolution operator matrices in the interaction picture are much smaller than in the Schrödinger picture for the chain.

C. Time evolution of matrix product states

After obtaining the chain Hamiltonian and the corresponding evolution operator in the interaction picture, one is ready to use a matrix product state to represent the wave function of the system and bath and apply the evolution operator to the MPS to compute dynamics. We briefly review the use of matrix product states and the time-evolution algorithm use here, namely, the time-evolution block-decimation method [7,38].

Given a state $|\psi(\sigma_s, \sigma_0, ..., \sigma_N)\rangle$ with N+2 spatially localized states $|\sigma_s\rangle$, $|\sigma_0\rangle$, $|\sigma_1\rangle$, ..., $|\sigma_N\rangle$ on sites s, 0, 1, ..., N, respectively (here s denotes a system), the MPS representation of this state is

$$|\psi\rangle = \sum_{\{\sigma_i\}} \sum_{\{a_i\}} \Gamma_{a_0}^{\sigma_s} S_{a_0} \Gamma_{a_0, a_1}^{\sigma_0} \cdots S_{a_N} \Gamma_{a_N}^{\sigma_N} |\sigma_1 \cdots \sigma_N\rangle. \quad (25)$$

Here $\{\sigma_i\}$ contains $\sigma_s, \sigma_0, \ldots, \sigma_N$ and $\{a_j\}$ contains a_0, \ldots, a_N . We refer to the labels of the sites' local states $\sigma_s, \sigma_0, \ldots, \sigma_N$ as physical legs. The diagonal matrices S_{a_i} in Eq. (25) are the singular values obtained by Schmidt decomposing the state $|\psi\rangle$ into a sum of direct product states in two subspaces spanned by $|\sigma_s, \ldots, \sigma_i\rangle$ and $|\sigma_{i+1}, \ldots, \sigma_N\rangle$, respectively.

The Hamiltonian of Eq. (21) includes long-range interactions. To evolve the state using the star Hamiltonian, one can use swap gates [14,39] to exchange positions of adjacent sites. A swap gate exchanges the two physical legs of two adjacent tensors. This exchange can be combined with an individual time evolution term and does not introduce additional computational cost if one properly orders the individual evolution terms and swap gates in the Trotter expansion of the entire evolution operator in Eq. (26) is the evolution operation used in practical calculations. It is formed by the combination of

individual evolution terms and swap gates:

$$U(t + \delta t, t)$$

$$= \hat{S}_{0,s}e^{-i[H_s + H_{s,0}(t + \delta t/4)]\delta t/2}$$

$$\times \hat{S}_{1,s}e^{-iH_{s,1}(t + \delta t/4)\delta t/2}\hat{S}_{2,s}e^{-iH_{s,2}(t + \delta t/4)\delta t/2}$$

$$\times \hat{S}_{3,s}e^{-iH_{s,3}(t + \delta t/4)\delta t/2} \cdot \cdot \cdot \hat{S}_{N-1,s}e^{-iH_{s,N-1}(t + \delta t/4)\delta t/2}$$

$$\times e^{-iH_{s,N}(t + \delta t/4)\delta t/2}e^{-iH_{s,N}(t + \delta t/4)\delta t/2}$$

$$\times S_{s,N-1}e^{-iH_{s,N}(t + \delta t/4)\delta t/2} \cdot \cdot \cdot \hat{S}_{s,3}e^{-iH_{s,3}(t + \delta t/4)\delta t/2}$$

$$\times \hat{S}_{s,2}e^{-iH_{s,2}(t + \delta t/4)\delta t/2}\hat{S}_{s,1}e^{-iH_{s,1}(t + \delta t/4)\delta t/2}$$

$$\times \hat{S}_{s,0}e^{-i[H_s + H_{s,0}(t + \delta t/4)]\delta t/2}. \tag{26}$$

Taking the first evolution step $e^{-i[H_s+H_{s,0}(t+\delta t/4)]\delta t/2}$ in Eq. (26) as an example, we show how this individual evolution term together with the swap gate $\hat{S}_{s,0}$ is incorporated in the relevant tensors of Eq. (25). The further evolution steps are applied in a similar way. This evolution term has four indexes because the Hamiltonian in the exponent is actually the sum of two tensor products of operators in the spaces of the system and the zeroth vibrational mode, namely $H_s \otimes \mathbb{1}_0$ and $A_s \otimes [d_0(t + \delta/4)\hat{b}_0 + \text{H.c.}]$. The components of this individual evolution term can be written as a rank-4 tensor $M_{ij}^{i'j'}$ in which i and i' are the indexes of the states in the system space, while j and j' are the indexes of states in the Hilbert space of the zeroth vibrational mode. The composite indexes (i',j') and (i, j) are the row and column indexes for the matrix representation of this individual evolution operator. To apply this individual evolution operator to the MPS of Eq. (25), we first contract the tensors $\Theta_{a_1}^{\sigma_s,\sigma_0} = \sum_{a_0,a_1} \Gamma_{a_0'}^{\sigma_s} S_{a_0',a_0} \Gamma_{a_0,a_1'}^{\sigma_0} S_{a_1',a_1}$. The contracted tensor describes the effective two-site wave function of the system site and the zeroth vibrational site. Note that σ_s and σ_0 are the indexes i and j that we used before. Thus $\Theta_{a_1}^{i',j'} = \Theta_{a_1}^{\sigma_s,\sigma_0}$. The next step is to contract the evolution term with the effective two site wave function $\tilde{\Theta}_{a_1}^{i',j'} = \sum_{ij} M_{ij}^{i',j'} \Theta_{a_1}^{ij}$, and apply the swap gate $\hat{S}_{s,0}$ to exchange the two physical legs i' and j': $\tilde{\Theta}_{a_1}^{i'j'} \to \tilde{\Theta}_{a_1}^{j'i'}$ and swapped effective wave function is then Schmidt decomposed: $\tilde{\Theta}_{a_1}^{j'i'} =$ $\sum_{a_0} \tilde{\Gamma}_{a_0}^{j'} \tilde{S}_{a_0} B_{a_0,a_1}^{i'} = \sum_{a_0} \tilde{\Gamma}_{a_0}^{\sigma_0} \tilde{S}_{a_0} B_{a_0,a_1}^{\sigma_s}$. The tensor $B_{a_0,a_1}^{\sigma_s}$ is then contracted with the inverse of $S_{a_1'a_1}$ to obtain the tensor $\tilde{\Gamma}_{a_0,a_1}^{\sigma_s} = \sum_{a_1'} B_{a_0,a_1'}^{\sigma_s} (S^{-1})_{a_1',a_1}, \text{ where } (S^{-1})_{a_1',a_1} = \delta_{a_1',a_1} S_{a_1 a_1}^{-1}.$ The gamma tensors $\tilde{\Gamma}_{a_0}^{j'}$, $\Gamma_{a_0,a_1}^{\tilde{\sigma_s}}$ and singular values \tilde{S}_{a_0} then replace the previous corresponding counterparts, which completes a single evolution step.

D. Scaling analysis

The three Hamiltonian schemes introduced in Sec. II have different computational costs. We present a qualitative scaling analysis to show the improved computational efficiency of the interaction-picture chain geometry (IC), compared to the chain geometry (C) scheme. We use $d_{\rm IC}$ and $d_{\rm C}$ to denote the energy levels (local dimensions) required for the IC schemes and the C scheme. $D_{\rm IC}$ and $D_{\rm C}$ are the bond dimensions (i.e., the number of important singular values) required for the IC and C scheme. In the MPS simulations of a typical open quantum system (e.g., the spin-boson model), the most

expensive step is the singular value decomposition (SVD) for tensors of size (d_1D_1, d_2D_2) , where d_1 and d_2 are the left and right local dimensions, while D_1 and D_2 are the left and right bond dimensions. For simplicity, we assume $D_1 = D_2$ and $d_1 \leq d_2$. The computational cost for such a SVD step is $\mathcal{O}((d_1D)^2d_2D) = \mathcal{O}(d_1^2d_2D^3)$. In the IC scheme, d_1 is the dimension of the system. For example, $d_1 = 2$ for a spin. Therefore, a SVD step in the IC scheme scales as $\mathcal{O}(4d_{\rm IC}D_{\rm IC}^3)$. Such a step in the C scheme scales as $\mathcal{O}(d_C^3 D_C^3)$ if we assume that the left and right local dimensions are identical. Section IV shows that the bond dimensions in the IC and C schemes usually satisfy a linear relationship: $D_{IC} = kD_C$, where k is generally larger than 1. Considering this linear relation, a SVD step in the C scheme scales as $\mathcal{O}((d_{IC}/k)^3D_{IC}^3)$. This means that, as long as $d_C^3 > 4k^3d_{IC}$, the IC scheme will be faster than the C scheme, at least for the SVD procedures. This condition is satisfied in many systems of physical and chemical interests. An example is the system studied in Sec. IV, which shows that k is 2–3 and $d_C/d_{IC} \approx 8$ –10 in the adiabatic cases. The scaling in the star geometry (S) is higher than in the IC scheme, regardless of the interaction strength because the entanglement (and hence the bond dimensions) grows rapidly with time (see Sec. IV). For general open quantum systems of interest in chemistry, the systems often involve a few electronic states (e.g., as in electron and energy transfer systems [40]), or can be mapped to a chain of coupled two-state systems [41,42], and the bath is composed of vibrational degrees of freedom with local dimensions that are much larger than the electronic degrees of freedom.

III. COMPUTATIONAL DETAILS

To demonstrate the efficiency of the method developed in Sec. II, we use the chain Hamiltonian Eq. (21) in the interaction picture and the corresponding Trotterized evolution operators with swap gates [Eq. (26)] to study a zero-bias spin-boson Hamiltonian. We compare the computational costs of this interaction-picture scheme to the chain and star geometries in the Schrödinger picture. The zero-bias spin-boson Hamiltonian is

$$egin{align} H &= \Delta \hat{\sigma}_x + \hat{\sigma}_z \otimes \int_{\Omega_0}^{\Omega_1} (\hat{a}^\dagger_\omega + \hat{a}_\omega) h(\omega) \, d\omega \ &+ \int_{\Omega_0}^{\Omega_1} \hat{a}^\dagger_\omega \hat{a}_\omega \omega \, d\omega, \end{gathered}$$

where Δ is the coupling between two states $|\uparrow\rangle$ and $|\downarrow\rangle$ and σ_x and σ_z are the Pauli matrices. We assume that the initial state of the spin-boson model is a product state $|\psi(t=0)\rangle = |\uparrow\rangle_s \otimes |0\rangle_0 \otimes |0\rangle_1 \otimes \cdots |0\rangle_N$. This choice follows from the initial equilibrium finite-temperature bath state in $\rho(0) = \rho_s \otimes e^{-\beta H_b}$ ($\beta = 1/k_B T$) that is mapped to the state of a zero-temperature bath by defining a temperature-dependent spectral density [17]. Following Ref. [43], we choose the Drude spectral density of the bath

$$J(\omega) = \frac{\eta \omega_c \omega}{\omega_c^2 + \omega^2},\tag{27}$$

where η is the coupling strength and ω_c is the characteristic frequency of the bath modes. The reorganization energy of the

TABLE I. Parameters. η_0 , ω_0 , and T_0 are unitless quantities that scale the system-bath coupling, the frequency of the bath, and the temperature of the bath, respectively.

Parameter	Physical quantity
Δ	Electronic coupling
$\eta = \eta_0 \Delta$	System-bath coupling
$\omega_c = \omega_0 \Delta$	Characteristic bath frequency
$k_BT = T_0\Delta$	Bath temperature
Ω_0 and Ω_1	Cutoff frequencies for the spectral density

spin-boson model is $\frac{4}{\pi} \int_0^\infty J(\omega)/\omega \, d\omega = 2\eta$ because the two spin states are coupled to the bath in opposite ways through the σ_z operator. The parameters used for the simulations of Sec. IV are shown in Table I. The ordering of sites in the star geometry plays a crucial role in the growth of the bond dimensions with time. In the star geometry, we order the bath sites based on the absolute values of their frequencies, with the lowest-frequency mode closest to the system (the spin). This ordering is used widely in MPS simulations of vibronic systems [6,22,44].

IV. RESULTS AND DISCUSSIONS

A. Spin-boson model in strong-coupling regimes

We now show the efficiency of the interaction-picture chain-geometry scheme (IC) using the spin-boson Hamiltonian in a strong-coupling regime at moderate to high temperatures. The dimensionless characteristic frequency ω_0 is set to be 0.25, 1.0, or 4.0, corresponding to the adiabatic, intermediate, and nonadiabatic regimes, respectively. The population dynamics at low temperatures, or in the weak-coupling regimes, are not studied here because they are relatively easy to simulate due to the low excitation of bath modes and the low entanglement, if no phase transition occurs.

1. Adiabatic regime: $\omega_c \ll \Delta$

In the adiabatic regime, the electronic coupling Δ is large compared to the characteristic frequency ω_c of the bath. We use a small characteristic frequency $\omega_0 = 0.25$ and a moderate temperature $T_0 = 1.0$ so that $\omega_c = \omega_0 \Delta = 0.25 \Delta$ and $T = T_0 \Delta = \Delta$. We plot the computed population evolution of the spin $|\uparrow\rangle$ state in Fig. 1. The dynamics are calculated by the three different schemes: the interaction-picture chain geometry (IC), the Schrödinger-picture chain geometry (C), and the star geometry (S). Each scheme uses various cutoffs for the dimension of the Hilbert space (local dimension) of the bath modes to show the convergence trends. The threshold for the singular values in the numerical simulations is 10^{-3} for all the simulations in this paper, unless otherwise noted. The maximum number of singular values is restricted to 1000. We also perform the simulations with a tighter threshold 10^{-4} (not shown). No significant difference between the simulation results with the two different thresholds was found, which indicates the results are converged with respect to the threshold of 10^{-3} for singular values. The dimensionless time step δt in all of the simulations is 5×10^{-2} , unless otherwise noted.

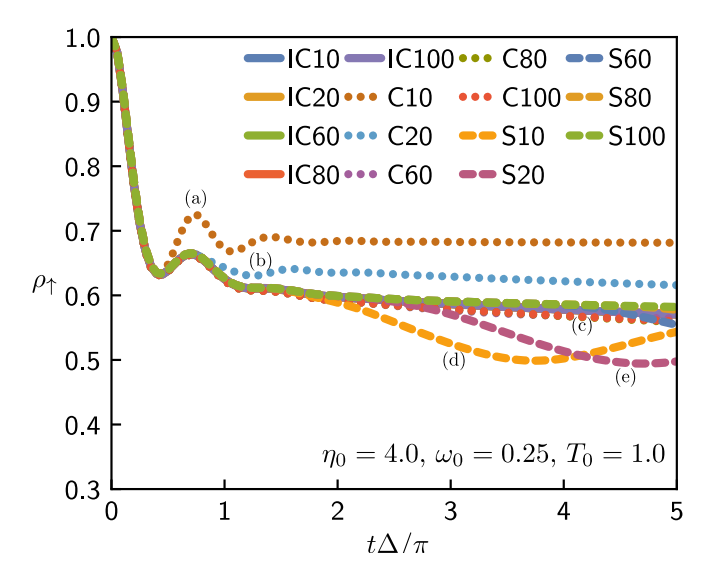


FIG. 3. Evolution of the $|\uparrow\rangle$ state population. "C," "IC," and "S" denote the chain geometry in the Schrödinger picture, the chain geometry in the interaction picture, and the star geometry in the Schrödinger picture, respectively. The numbers 10, 20, etc. are the maximum numbers (cutoff) of energy levels for each single bath mode. (a) C10 is not converged. (b) C20 is not converged. (c) C60, IC10-80, and S60-100 are converged except for the tail of S60. (d) S10 and (e) S20 are not converged. For the results in S and C, better convergence is achieved with larger local dimensions. The cutoff frequencies for the spectral density, Ω_0 and Ω_1 , are $\mp 6.36\Delta$.

As shown in Fig. 3, the simulations for the chain geometry or the star geometry (denoted C and S) in the Schrödinger picture deviate from the converged results obtained in the interaction-picture chain geometry (denoted IC), unless a sufficiently large cutoff for the bath-mode Hilbert space (the local dimension) is used. We find that a cutoff of 10 for the local dimension is sufficient for the IC scheme to converge and a cutoff of 60–80 is required to ensure convergence in the C scheme. The cutoff of 80 needed for the S scheme is much less favorable than both IC and C schemes.

To further explore the differences among the three schemes, Fig. 4 shows the growth of bond dimensions during the simulations of Fig. 3, with different cutoffs for the local dimensions. The results in the adiabatic regime show that the growth in the bond dimensions has different patterns in the three schemes. The slowest bond-dimension growth occurs in the interaction-picture chain geometry (IC) and the Schrödinger-picture chain geometry (C). The fastest growth occurs in the star geometry. Compared to the Schrödinger picture chain geometry, the interaction-picture chain scheme exhibits a similar growth pattern of the bond dimensions, but involves much smaller matrices as discussed in Sec. I. This slow growth of bond dimensions occurs because the time-dependent interactions in the IC scheme exhibit a traveling-wave pattern as shown in Fig. 5. Furthermore, the interactions are delocalized among multiple modes, and each interaction is weaker than the system-bath interaction in the Schrödinger-picture chain.

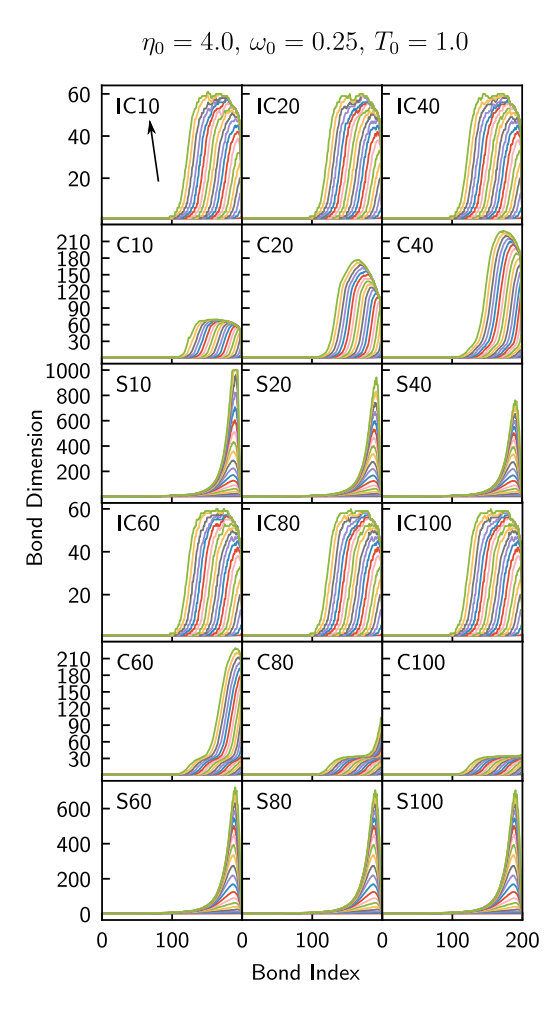


FIG. 4. Growth of bond dimensions in the IC, C, and S schemes. The meanings of the labels (IC10, etc.) are given in the caption of Fig. 3. The horizontal axis is the index of the bond between every neighboring two sites on the MPS. The vertical axis is the number of singular values, i.e., the bond dimension. The last bond (index 200) is the bond between the spin and the first bath mode. In each panel, curves in different colors represent the bond dimensions at different times and the bond dimensions grow from zero at the time zero to a larger value at the time $t\Delta/\pi=5$. The arrow points to the direction of the growth (also the direction of time). The bond dimensions grow as time proceeds (the direction of the arrow) and the growth of bond dimensions in the S scheme is much faster than in the IC and C schemes.

2. Intermediate regime: $\omega_c \sim \Delta$

In the intermediate regime, the magnitude of the characteristic frequency ω_c of the bath modes is comparable to the electronic coupling. We set $\omega_0 = 1.0$ so $\omega_c = \omega_0 \Delta = \Delta$. If the same temperature value $T_0 = 1.0$ is chosen as in the adiabatic case, we expect that the occupations in the bath modes will be lower than in the adiabatic case because a higher frequency ($\omega_0 = 1.0$) is set in the intermediate regime. To make the comparisons between the different schemes more distinct, the dimensionless temperature is set to $T_0 = 2.0$, which is higher than the temperature studied in the adiabatic regime. This higher temperature is more costly for the simulations than the low-temperature regimes because high-lying states

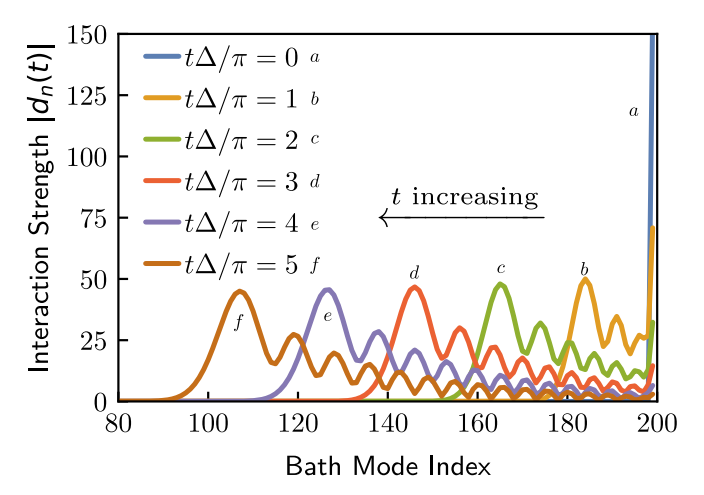


FIG. 5. Absolute value of the complex-valued interaction strengths $d_n(t)$, where n is the index for the bath modes. The blue line (labeled by a) is $d_n(t=0)$ and the spin only interacts with the first mode (index 200) at this moment. The rest of the colors (labeled by b,..., and f) are the interaction strength at later times. The time-dependent $|d_n(t)|$ exhibits a traveling-wave pattern and at different moments the largest interaction strength occurs at different modes. Qualitatively, the large interaction strength at t=0 is distributed into multiple modes at later times. This explains the low bath mode excitation and the slow growth of bond dimensions in the interaction picture. The lower and upper limits Ω_0 and Ω_1 of the spectral density determine the velocity of the traveling wave.

of the bath are populated. The computed population dynamics are shown in Fig. 6. In the IC scheme, a converged result is found with a small cutoff for the local dimensions of the bath modes. This result is similar to the situation in the adiabatic regime. However, the C and S schemes in the intermediate coupling regime converged more rapidly with respect to local

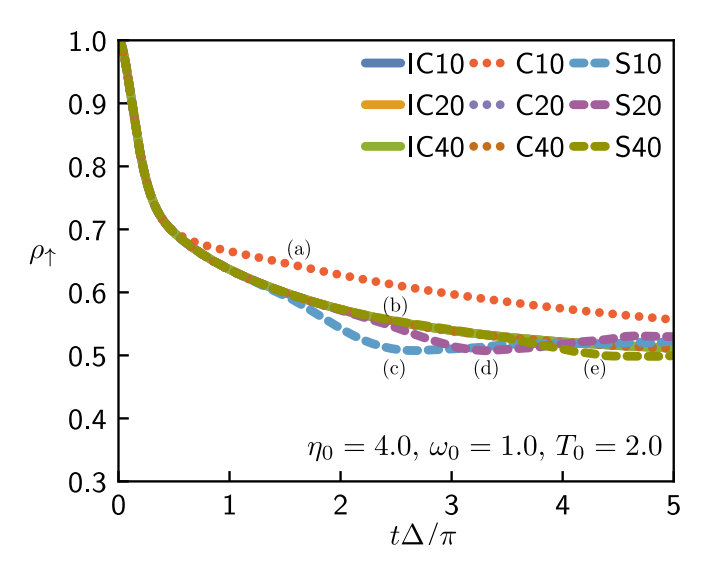


FIG. 6. Evolution of state $|\uparrow\rangle$ population. The threshold for singular values is 10^{-4} . The dimensionless time step δt is 5×10^{-3} . The cutoff frequencies Ω_0 and Ω_1 for the spectral density are $\mp 12.74\Delta$. (a) C10 is not converged. (b) IC10, IC20, IC40, C20, and C40; all are converged. (c) S10 is not converged. (d) S20 is not converged. (e) S40; almost converged except for the part from $t\Delta/\pi=3.5$ to 5.

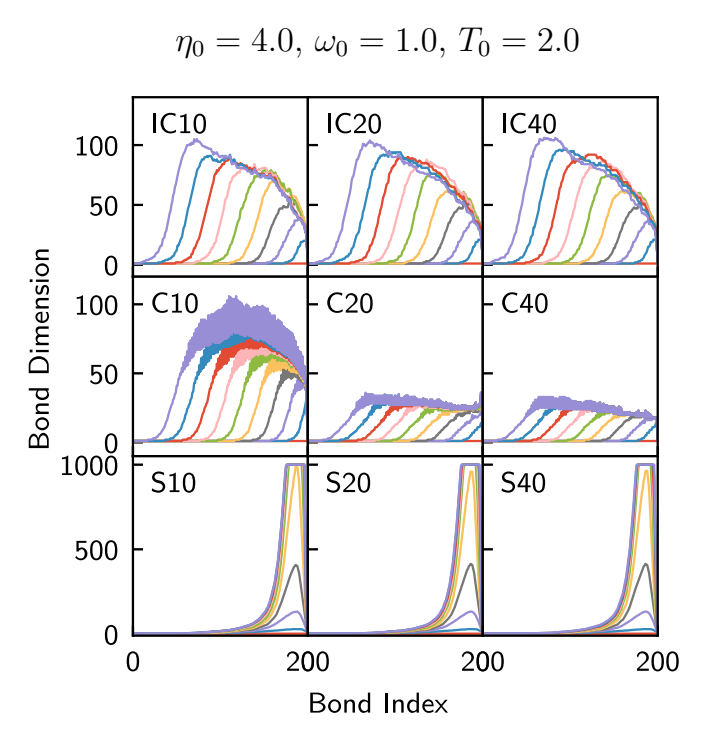


FIG. 7. Growth of bond dimensions in the Schrödinger-picture chain geometry (middle panel), the interaction-picture chain geometry (top panel), and the Schrödinger-picture star geometry (bottom panel), in the intermediate regimes.

dimensions than in the adiabatic regime. This milder requirement for local dimensions occurs because the frequencies of the modes are comparable to the off-diagonal coupling of the spin (the system) and fewer energy levels of the modes are excited than in the adiabatic (small frequencies) case. The low mode excitations are also caused by the fact that the ratio between the characteristic frequency and the temperature in the intermediate regime ($\omega_0/T_0=0.5$) is twice of that in the adiabatic regime ($\omega_0/T_0=0.25$). Although the requirement for local dimensions is less demanding for all the schemes compared to the adiabatic case, the IC scheme considerably outperforms the C and S schemes, benefiting from the reduced matrix and tensor sizes by requiring a smaller cutoff of local bath dimensions in the intermediate regime. The IC scheme can become more efficient as the temperature grows. A considerable number of electron-transfer [45], singlet-fission [46], and excitation-energy-transfer (EET) systems [12,47] fall in this intermediate regime, where the magnitude of the electronic coupling is comparable to vibrational frequencies. We expect that the IC scheme can accelerate MPS simulations for chemical systems of interest in this regime [48].

The entanglement of each bond is explored in Fig. 7, which shows the growth of bond dimensions for the simulations of Fig. 6. As in the adiabatic cases, the IC and C schemes have similar growth patterns of bond dimensions as long as the results in the C scheme have converged (e.g., C20 and C40), although the IC scheme has slightly faster growth of bond dimensions (twice as fast as in C). The similarity of the C and IC scheme on the growth pattern of bond dimensions shows the similar kinds of energy flow through the bath chain, which is due to the traveling-wave pattern of the time-dependent

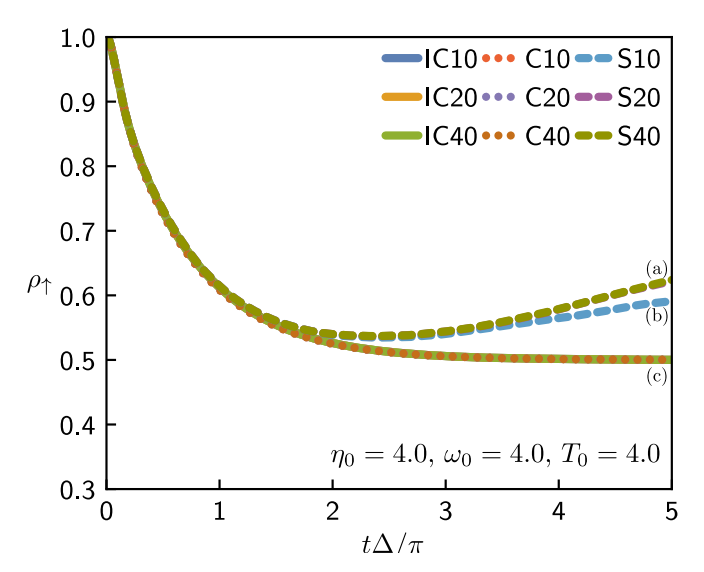


FIG. 8. Time evolution of the state $|\uparrow\rangle$ population in the nonadiabatic regimes. The threshold for singular values is 10^{-3} . The dimensionless time step δt is 1.25×10^{-2} . (a) S40 and S20, not converged. (b) S10, not converged. This is because the bond dimension in the S scheme grows extremely rapidly and the current threshold (10^{-3}) for the singular values is not enough for accuracy. (c) IC10, IC20, IC40, C10, C20, and C40. The dynamics in the IC and C schemes are converged using a small local dimension (10), while the S scheme does not yield converged results regardless of the number of vibrational levels used here. The cutoff frequencies Ω_0 and Ω_1 for the spectral density are $\mp 31.83\Delta$.

interactions in the IC scheme (see Fig. 5). For the S scheme, although the dynamics are converged, the bond dimensions still grow rapidly because of the intrinsic structure of the MPS in the star geometry. This finding indicates that the structure of MPS in the S scheme is not optimal, since the spin interacts with all of the modes at any time.

3. Nonadiabatic regime: $\omega_c \gg \Delta$

In the nonadiabatic regime, we set the characteristic frequency ω_c of the bath modes to be $\omega_c = 4\Delta$ and the temperature to be $T = T_0 \Delta = 4.0 \Delta$. In this regime, the simulations do not require too many bath-mode energy levels for the calculations to converge. No significant deviations are shown in the IC and C schemes, regardless of the local dimension cutoffs. However, the S scheme shows deviations due to the rapid growth of entanglement for the star geometry (see Fig. 8 and Fig. 9). Although the IC and C schemes do not show significant differences as we vary local dimensions (for the temperature used), we expect the IC scheme can benefit in speed from the smaller matrices and the smaller local dimensions in the IC scheme. The smaller matrices in the IC scheme may also improve the speed of numerical simulations for low-temperature regimes where the classical Marcus rate theory does not apply and the nonadiabatic rate is sensitive to details of the spectral density [49].

B. Computational efficiencies in the interaction picture

The numerical simulations described here show that the IC scheme requires fewer bath energy levels than the C scheme

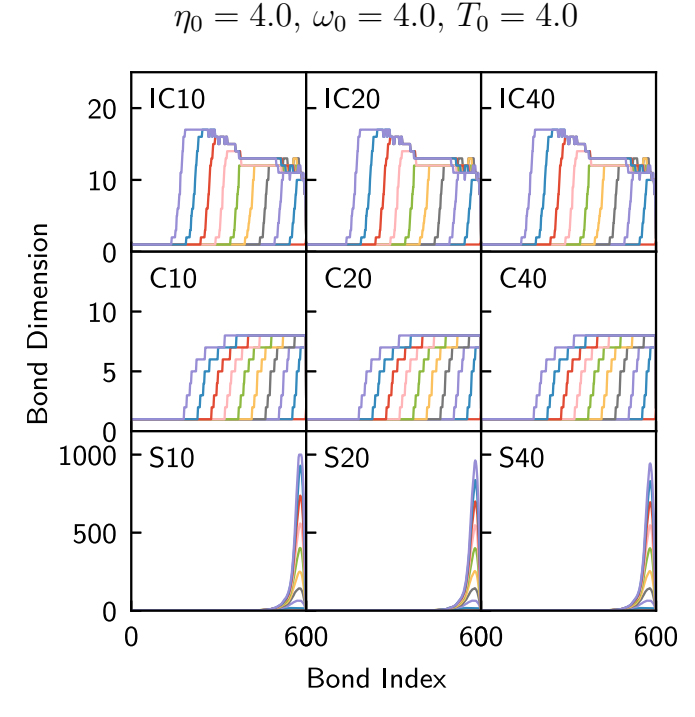


FIG. 9. Growth of bond dimensions in the nonadiabatic regimes for the Schrödinger-picture chain geometry (middle panel), the interaction-picture chain geometry (top panel), and the Schrödinger-picture star geometry (bottom panel).

to obtain converged results in the adiabatic, strong-coupling, high-temperature regimes. Using the scaling relations of Sec. II D, we analyze the simulations of Fig. 4 (i.e., the adiabatic spin-boson model). We find that $D_{\rm IC}\approx 2D_{\rm C}$, $d_{\rm C}=80$, and $d_{\rm IC}=10$. As a result, the scaling of a single SVD step in the C scheme is $\mathcal{O}(80^3D_{\rm C}^3)=\mathcal{O}(51200D_{\rm C}^3)$ and the scaling in the IC scheme is $\mathcal{O}(4\times10\times8D_{\rm C}^3)=\mathcal{O}(320D_{\rm C}^3)$. The findings indicate that the IC scheme is roughly 1600 times faster than the C scheme for the SVD operations. If we assume $D_{\rm C}\approx 2D_{\rm IC}$, the C scheme is faster than the IC scheme $[\mathcal{O}(4d_{\rm IC}D_{\rm IC}^3)<\mathcal{O}(d_{\rm C}^3D_{\rm C}^3)]$ only if $d_{\rm C}^3<32d_{\rm IC}$. This relation means that if the local dimension for a bath mode is larger

than $6 \ (\approx \sqrt{32})$, one should use the interaction-picture chain geometry (IC scheme), at least for the two-site propagation methods (e.g., TEBD and TDVP1). In addition, upon the interaction-picture transformation, the requirement for local dimensions of the bath modes are reduced, improving the tensor contraction efficiency. The computational advantages of the interaction picture depend on the propagation methods that are used to compute the dynamics. The improvement is more substantial for two-site methods. The one-site methods (e.g., TDVP1) may benefit less from the interaction-picture transformation because these methods depend on only one local dimension, while the two-site methods depend on the product of two local dimensions.

For the star geometry (the S scheme), the SVD step also scales as $\mathcal{O}(4d_SD_S^3)$, but D_S is often a large number. As a result, the S scheme is always slower than the IC scheme.

V. CONCLUSIONS AND OUTLOOK

By transforming the chain Hamiltonian to the interaction picture, we developed a numerical approach that outperforms the conventional chain-geometry and star-geometry approaches in the regimes of moderate-to-strong couplings and intermediate-to-high temperatures. The efficiency of this approach is demonstrated by simulating the spin-boson model and comparing the growth of bond dimensions to the conventional approaches. The results indicate that the interaction-picture approach gains increased efficiency in simulating open quantum systems with boson environments using the t-DMRG method, especially when the population of the excitated boson states are high. Possible extensions of this interaction-picture approach could include anharmonic baths, the combination with the optimized-boson-basis (OBB) or the local-basis-optimization (LBO) approach [36,50,51] to further accelerate singular value decomposition, and the use of the polaron transformation [52–55] to further reduce entanglement in the interaction picture.

ACKNOWLEDGMENT

This material is based upon work supported by the National Science Foundation under Grant No. 1925690.

^[1] S. R. White, Phys. Rev. Lett. 69, 2863 (1992).

^[2] S. R. White, Phys. Rev. B 48, 10345 (1993).

^[3] S. Yan, D. A. Huse, and S. R. White, Science 332, 1173 (2011).

^[4] S. R. White and A. E. Feiguin, Phys. Rev. Lett. 93, 076401 (2004).

^[5] A. J. Daley, C. Kollath, U. Schollwöck, and G. Vidal, J. Stat. Mech. Theory Exp. 2004, P04005 (2004).

^[6] X. Xie, Y. Liu, Y. Yao, U. Schollwöck, C. Liu, and H. Ma, J. Chem. Phys. 151, 224101 (2019).

^[7] G. Vidal, Phys. Rev. Lett. 91, 147902 (2003).

^[8] I. Affleck, T. Kennedy, E. H. Lieb, and H. Tasaki, Phys. Rev. Lett. 59, 799 (1987).

^[9] I. Affleck, T. Kennedy, E. H. Lieb, and H. Tasaki, Commun. Math. Phys. 115, 477 (1988).

^[10] U. Schollwöck, Ann. Phys. (NY) 326, 96 (2011).

^[11] T. D. Kühner, S. R. White, and H. Monien, Phys. Rev. B 61, 12474 (2000).

^[12] P. Huo and D. F. Coker, J. Phys. Chem. Lett. 2, 825 (2011).

^[13] B. R. Landry and J. E. Subotnik, J. Chem. Phys. 137, 22A513 (2012).

^[14] E. Stoudenmire and S. R. White, New J. Phys. 12, 055026 (2010).

^[15] M. L. Wall, A. Safavi-Naini, and A. M. Rey, Phys. Rev. A 94, 053637 (2016).

^[16] F. A. Wolf, I. P. McCulloch, and U. Schollwöck, Phys. Rev. B 90, 235131 (2014).

^[17] D. Tamascelli, A. Smirne, J. Lim, S. F. Huelga, and M. B. Plenio, Phys. Rev. Lett. 123, 090402 (2019).

^[18] I. de Vega and M.-C. Banuls, Phys. Rev. A **92**, 052116 (2015).

- [19] J. Prior, A. W. Chin, S. F. Huelga, and M. B. Plenio, Phys. Rev. Lett. 105, 050404 (2010).
- [20] I. de Vega, U. Schollwöck, and F. A. Wolf, Phys. Rev. B 92, 155126 (2015).
- [21] M. Sánchez-Barquilla and J. Feist, Nanomaterials 11, 2104 (2021).
- [22] R. Borrelli and M. F. Gelin, WIREs Comput. Mol. Sci. 11, e1539 (2021).
- [23] M. Brenes, J. J. Mendoza-Arenas, A. Purkayastha, M. T. Mitchison, S. R. Clark, and J. Goold, Phys. Rev. X 10, 031040 (2020)
- [24] G. Pleasance and F. Petruccione, arXiv:2108.05755.
- [25] A. Purkayastha, G. Guarnieri, S. Campbell, J. Prior, and J. Goold, Phys. Rev. B 104, 045417 (2021).
- [26] P. Bhattacharyya and G. R. Fleming, J. Phys. Chem. Lett. 11, 8337 (2020).
- [27] Y. Wang and J. Y. Haw, Phys. Lett. A 379, 779 (2015).
- [28] A. Moroz, Ann. Phys. (NY) 340, 252 (2014).
- [29] P. Forn-Díaz, L. Lamata, E. Rico, J. Kono, and E. Solano, Rev. Mod. Phys. 91, 025005 (2019).
- [30] A. J. Dunnett and A. W. Chin, Front. Chem. 8, 2296 (2021).
- [31] A. W. Chin, Á. Rivas, S. F. Huelga, and M. B. Plenio, J. Math. Phys. 51, 092109 (2010).
- [32] R. Rosenbach, Ph.D. thesis, Universität Ulm, 2016.
- [33] X. Bian, Y. Wu, H.-H. Teh, Z. Zhou, H.-T. Chen, and J. E. Subotnik, J. Chem. Phys. 154, 110901 (2021).
- [34] Y. Wu and J. E. Subotnik, Nat. Commun. 12, 700 (2021).
- [35] D. Segal, A. J. Millis, and D. R. Reichman, Phys. Rev. B 82, 205323 (2010).
- [36] C. Brockt, F. Dorfner, L. Vidmar, F. Heidrich-Meisner, and E. Jeckelmann, Phys. Rev. B 92, 241106(R) (2015).
- [37] T. Lacroix, A. Dunnett, D. Gribben, B. W. Lovett, and A. Chin, Phys. Rev. A **104**, 052204 (2021).

- [38] Y.-Y. Shi, L.-M. Duan, and G. Vidal, Phys. Rev. A **74**, 022320 (2006).
- [39] J. Biamonte and V. Bergholm, arXiv:1708.00006.
- [40] J. N. Onuchic, D. N. Beratan, and J. Hopfield, J. Phys. Chem. 90, 3707 (1986).
- [41] M. Schröter, S. D. Ivanov, J. Schulze, S. P. Polyutov, Y. Yan, T. Pullerits, and O. Kühn, Phys. Rep. **567**, 1 (2015).
- [42] T. Holstein, Ann. Phys. (NY) 8, 325 (1959).
- [43] M. Thoss, H. Wang, and W. H. Miller, J. Chem. Phys. 115, 2991 (2001).
- [44] J. Ren, Z. Shuai, and G. Kin-Lic Chan, J. Chem. Theory Comput. 14, 5027 (2018).
- [45] H. Tamura, R. Martinazzo, M. Ruckenbauer, and I. Burghardt, J. Chem. Phys. 137, 22A540 (2012).
- [46] Y. Fujihashi and A. Ishizaki, J. Phys. Chem. Lett. 7, 363 (2016).
- [47] A. Ishizaki and G. R. Fleming, J. Chem. Phys. 130, 234111 (2009).
- [48] N. Christensson, H. F. Kauffmann, T. Pullerits, and T. Mancal, J. Phys. Chem. B 116, 7449 (2012).
- [49] R. Egger, C. Mak, and U. Weiss, J. Chem. Phys. 100, 2651 (1994).
- [50] C. Guo, A. Weichselbaum, J. von Delft, and M. Vojta, Phys. Rev. Lett. 108, 160401 (2012).
- [51] F. A. Y. N. Schröder and A. W. Chin, Phys. Rev. B 93, 075105 (2016).
- [52] R. Silbey and R. A. Harris, J. Chem. Phys. **80**, 2615 (1984).
- [53] D. Zueco and J. García-Ripoll, Phys. Rev. A 99, 013807 (2019).
- [54] T. Shi, Y. Chang, and J. J. García-Ripoll, Phys. Rev. Lett. 120, 153602 (2018).
- [55] S. He, L. Duan, and Q.-H. Chen, Phys. Rev. B **97**, 115157 (2018).